ORIGINAL PAPER

physica status solidi
www.pss-b.com
Check for updates

Designing "Metamolecules" for Photonic Function: Reduced Backscattering

*Tian-Song Deng, John Parker, Yutaro Hirai, Nolan Shepherd, Hiroshi Yabu, and Norbert F. Scherer**

Metamaterials, subwavelength nanostructured materials, can exhibit novel optical properties such as a negative index of refraction. Dielectric core–nanoparticle satellite clusters, termed "metamolecules," can have strong optical magnetic resonances in the visible wavelength range—a requirement to achieve negative refractive index materials. However, achieving the desired photonic properties is challenging due to limited control in forming the metamolecule structures. Here, polystyrene (PS) core–gold nanoparticle (AuNP) satellite metamolecules with highly ordered single layers (monolayers) of AuNPs are fabricated and single particle spectroscopy, electron tomography structural measurements, and electrodynamics simulations are conducted to study the photonic properties of metamolecules constituted of $\approx$100 AuNPs. The simulated and experimental spectra of the many metamolecules studied, including excitation with azimuthally and radially polarized light, are in excellent agreement. It is shown that the scattering properties of the metamolecules are dominated by the AuNPs near the "equator" of the cluster, and that backscattering is strongly suppressed when different multipolar modes (e.g., dipolar and quadrupolar) of electric or optical magnetic character have comparable intensity due to the π-phase shift of their scattering. Both the optical excitation fields and the ordering of the nanoparticles within metamolecules affect their optical excitation and scattering properties, providing new insights into designing novel photonic metamaterials.

1. Introduction

Special optical properties, including a negative refractive index, large absorption cross-sections, and small backscattering,[1–3] make metamaterials desirable for many applications such as creating invisibility cloaks, enhanced sensors, and nanolasers and solar energy collection.[2,4–10] Metasurfaces are readily fabricated by top-down lithography.[4,5] However, the grain boundaries and

defects within the resulting nanostructures cause greater damping and concomitantly impair their optical properties. On the other hand, bottom-up approaches to fabricate metamaterials can utilize highly crystalline metallic nanoparticles (e.g., gold and dielectrics) as building blocks.[11–22] For example, core–satellite clusters or "metamolecules" have been fabricated in this manner.[12,15,19–21] A metamolecule can consist of a dielectric particle (e.g., polystyrene (PS) or SiO_2) "core" and metallic nanoparticles functionalized to it as "satellites."[12,15,20] An interesting suggestion is that metamaterials fabricated from metamolecules can exhibit a negative refractive index in the visible and NIR wavelength range and would be "natural" constituents of 3D metafluids.[12]

While core–satellite metamolecules are readily prepared by self-assembly, achieving reproducible optical properties is challenging. UV–vis–NIR extinction measurements reveal broad peaks in their ensemble optical spectra. By contrast, single particle (scattering) measurements of individual metamolecules give sharper spectra, but with significant variation from metamolecule to metamolecule.[20] Structural characterization by scanning or transmission electron microscopy (SEM or TEM) reveals only partial information about the metamolecule structures.[12,15,20] Therefore, detailed understanding of the optical properties of core–satellite metamolecules has not been possible to date for three main reasons. First, the inhomogeneous arrangements of the nanoparticle satellites around the dielectric core (e.g., short chains of nanoparticles and aggregates of nanoparticles) can cause intense

Dr. T.-S. Deng,[+] Dr. N. Shepherd, Prof. N. F. Scherer
The James Franck Institute
University of Chicago
929 E 57th Street, Chicago, IL 60637, USA
E-mail: nfschere@uchicago.edu

The ORCID identification number(s) for the author(s) of this article can be found under https://doi.org/10.1002/pssb.202000169.

[+]Present address: School of Electronics and Information Engineering, Hangzhou Dianzi University, No. 1158, 2nd Avenue, Baiyang Street, Hangzhou 310018, China

Dr. J. Parker, Dr. N. Shepherd, Prof. N. F. Scherer
Department of Chemistry
University of Chicago
929 E 57th Street, Chicago, IL 60637, USA

Dr. J. Parker
Department of Physics
University of Chicago
929 E 57th Street, Chicago, IL 60637, USA

Dr. Y. Hirai, Prof. H. Yabu
WPI–Advanced Institute for Materials Research (AIMR)
Tohoku University
2-1-1, Katahira, Aoba-ku, Sendai 980-8577, Japan

ADVANCED
SCIENCE NEWS
www.advancedsciencenews.com

physica
pssb
status solidi

www.pss-b.com

redshifted scattering spectra and broadened plasmonic resonances.[20] Second, conventional electron microscopy (e.g., TEM) only gives a 2D projection of the 3D metamolecule. While the 2D projection is adequate for estimating the structure of simple 2D systems, such as dimers and rings,[23–25] in the case of 3D objects (e.g., core–satellite clusters), a single 2D projected image is insufficient to accurately obtain their 3D structure. This inadequacy becomes manifest by performing electrodynamics simulations of the assumed structure and comparing the experimental and simulated spectroscopic results.[20,26] The unknown mismatch of the actual and simulated structures gives rise to the inconsistency of the experimental and simulated spectra. Third, the usual way to excite the metamolecules is with linearly polarized light, where the polarization is spatially homogeneous. However, these scalar beams have little selectivity for excitation or study of electric versus magnetic modes.[20,26]

In our previous work,[20] single particle scattering spectroscopy measurements were performed using optical vector beams to illuminate individual SiO_2–Ag nanoparticle core–satellite nanoclusters (metamolecules). We showed that focused vector beams allow selective excitation of collective optical magnetic modes.[20,26] TEM images were taken and the number of Ag nanoparticles was counted and used to build a model structure for finite-difference time-domain (FDTD) simulations. In these

simulations, we assumed that the Ag nanoparticles were randomly packed (or well ordered) on the surface of the SiO_2 core. Although we found that electric modes or magnetic modes could be selectively excited by radially or azimuthally polarized light, respectively, the simulated spectra were only in modest agreement with the experimental spectra. In addition, we also found the simulated spectra varied considerably with different structural permutations of the Ag nanoparticle arrangements.[20,26] A strong scattering peak at ≈900 nm was observed in some experimental spectra, but not in FDTD simulations. We attributed it to the formation of short "chains" of Ag nanoparticles with sub-nanometer gaps (nearly touching). Due to computational restrictions of interparticle separations (>2 nm), this peak was not captured in FDTD simulations. We concluded that the inconsistencies arose from the lack of specific knowledge of the 3D structures, which conventional TEM measurements cannot provide, and therefore incompletely informed simulations: That is, the modeled 3D structures were significantly different from the actual nanoparticle locations in the metamolecule.

In this article, we have substantially enhanced the state of the art on understanding spectroscopic properties of novel metamolecule structures: Specifically, all the aforementioned shortcomings of metamolecule fabrication, characterization, and simulation are addressed here. **Figure 1** shows the procedure
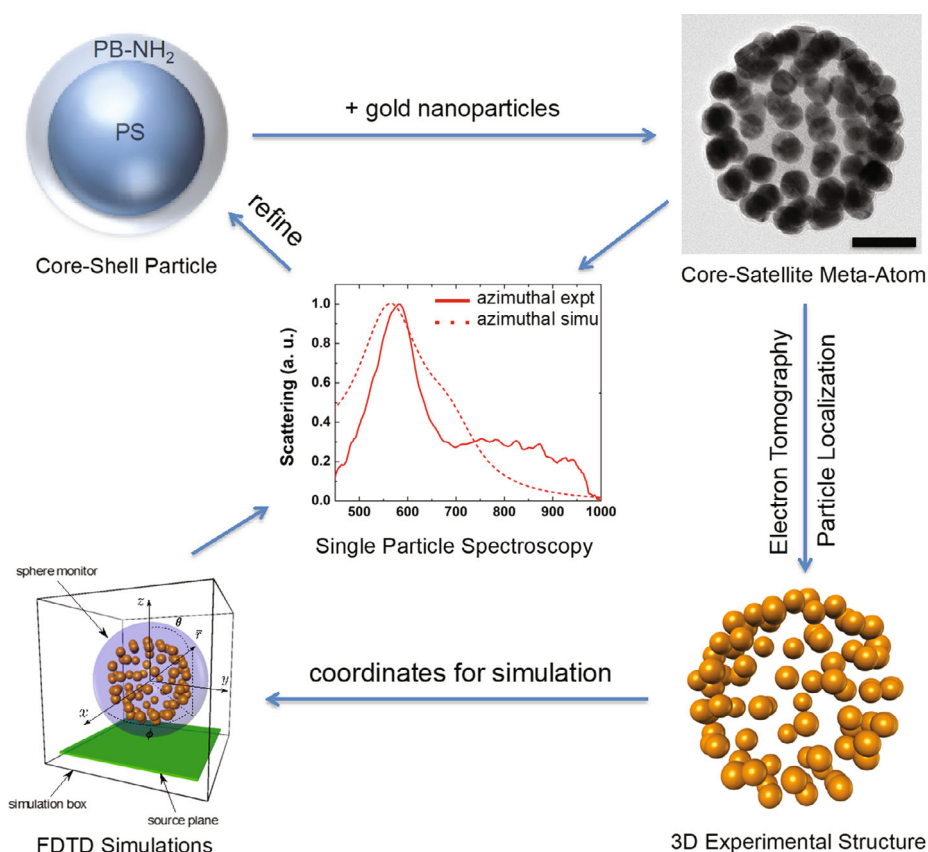

Figure 1. Approach for exacting studies of core–satellite metamolecules. To fully understand the structures and optical properties of the same metamolecule both in experimental measurements and simulations, we devised the approach shown that includes 1) PS–NH₂ core–shell particle preparation; 2) metamolecule preparation, scale bar = 50 nm; 3) single particle spectroscopy; 4) electron tomography and particle localization; and 5) electrodynamics simulations.

**ADVANCED
SCIENCE NEWS**
www.advancedsciencenews.com

pss b
physica status solidi b
www.pss-b.com

of our comprehensive approach. We fabricate PS–AuNP core–satellite metamolecules and study them systematically via single particle spectroscopy, electron tomography and 3D particle localization, and FDTD simulations. The latter are now based on the 3D coordinates of all AuNPs in the structures. Specifically, we prepare PS–AuNP core–satellite metamolecules where the AuNPs are well separated (i.e., not touching each other). We perform single particle spectroscopy using both linearly polarized light *and* vector beams. We use *electron tomography* (in both TEM and STEM modes), 3D reconstruction, and particle localization to obtain the detailed 3D structural information of the measured metamolecules. This structural characterization includes obtaining the diameter and 3D coordinates of the center of each nanoparticle. These very complete characterizations allow exacting comparisons with electrodynamics simulations of 3D core–satellite clusters using the 3D experimental data. By combining these results, we systematically study the photonic properties of individual PS–AuNP metamolecules containing about 100 or more AuNPs. We also examine the backward and forward scattering of the metamolecules by simulation. We find that backscattering can be controlled by directional interference of collective electric and magnetic modes of the metamolecules that can be selectively excited with the various types of scalar and vector beams used.

2. Results and Discussion

2.1. Metamolecule Fabrication and Single Particle Spectroscopy

The core–satellite metamolecules were synthesized using our previously reported method with slight modification.[19] Briefly, core–shell particles consisting of PS and amino-terminated 1,2-polybutadiene (PB-NH$_2$) were prepared by i) self-organized precipitation (SORP) and then AuNPs were introduced by ii) heterocoagulation and iii) diffusion. When aqueous dispersions of positively and negatively charged nanoparticles are mixed, metamolecules are formed through electrostatic interactions. Recently, we fabricated metamolecules from aqueous dispersions of PB-NH$_2$ and AuNPs.[27] AuNPs diffuse into the interior of the PB-NH$_2$ particles when the molecular weight of the PB-NH$_2$ is sufficiently low. As the thicknesses of PB-NH$_2$ shell layers of core–shell particles strongly depends on the PB-NH$_2$ content, the adsorption layer of AuNPs increases with increasing PB-NH$_2$ content and decreasing PS content. Thus, one can obtain monolayer and multilayer metamolecules by controlling the PS:PB-NH$_2$ ratio. We also studied different sizes of AuNPs: metamolecules made from 20 or 30 nm dia. AuNPs. Further details are given in the Experimental Section. Typical TEM images of the PS–AuNP metamolecules are shown in Figure S1, Supporting Information, and Figure 1.

Single particle scattering spectra were measured using a home-built microscopy setup that was integrated with a fiber continuum laser and optics for broadband vector beam spectroscopy. The vector beam spectroscopy setup is described in detail elsewhere.[20,25] Briefly, a broadband coherent white light continuum (Fianium: emitting between 450 and 1000 nm) was coupled to an inverted optical microscope (Olympus, IX-81) equipped with a 100× oil immersion objective with numerical aperture, numerical aperture (NA) ≤ 1.4 (SAPO 100×). Either conventional linearly polarized light or vector beams (azimuthally or

radially polarized) were used. The broadband azimuthal and radial beams were created using a vector beam generator (ARCoptix), a liquid-crystal-based polarization converter that uses twisted nematic liquid crystals sandwiched between one uniform and one circularly rubbed alignment layer.[28] The collimated beam was reflected by a 50/50 beam splitter and focused by the oil immersion objective onto the metamolecules supported on a TEM grid inside a liquid-filled sample cell. The backscattered light was used to record images and spectra of the sample plane using a complementary metal oxide semiconductor (CMOS) camera (Andor, Neo) and a spectrometer CCD array detector (Andor Shamrock and Newton EMCCD detector). Additional details are provided in the Experimental Section and Manna et al.[20]

We conducted correlated single-particle spectroscopy and structure measurements of specific metamolecules. Survey TEM images were acquired before taking scattering spectra to identify good candidates for spectroscopic study. Following the TEM measurements, the grid was placed on a glass cover slide, and glycerol ($n = 1.47$) was put on top of the grid to match the index of the glass slide and formvar-coated TEM grid. The sample cell was closed with another cover slide on the top, forming a sandwiched structure, with the grid between the two glass slides. Note that the metamolecules chosen for optical measurements were well separated from others (by at least 5 μm) to avoid scattering from neighboring metamolecules that could affect the spectra.

After completing the optical measurements on a set of metamolecules, the glycerol was removed by drying the TEM grid in vacuum overnight. The set metamolecules were imaged in TEM at higher resolution. We conducted electron tomography on select individual metamolecules and performed particle localization analysis[29] to get the 3D coordinates (and diameter) of each AuNP. We did this by acquiring a tilt series of TEM images in bright field mode or in high-angle annular dark-field scanning transmission electron microscopy (HAADF-STEM) mode, with tilt angles from 70° to −70°, with a step size of 1°. Tomographic reconstruction of the images was done with the IMOD software package using the simultaneous iterative reconstruction technique (SIRT).[30] We used a 3D particle localization code developed by Crocker and Grier[29] to determine the coordinates of the center and diameter of each particle. This gives us the complete 3D structural information of these complex structures that contain about 100 AuNPs. More details concerning the electron tomography and particle localization can be found in the Experimental Section and Supporting Information.

Figure 2a shows an ≈150 nm dia. metamolecule consisting of 20 nm dia. (average size) AuNPs. Figure 2b shows the equatorial plane of the metamolecule (after reconstruction), showing that it is a monolayer structure. Figure 2c shows the 3D structure of the metamolecule after 3D particle localization. In this particular metamolecule, 76 AuNPs were found. The detailed 3D structural information allows more complete understanding of the self-assembly process, and is used in FDTD simulations to theoretically analyze the collective plasmonic and optical magnetic properties of the metamolecules.

2.2. Electrodynamics Simulations

We performed electrodynamics simulations of the monolayer metamolecule using the experimental 3D structural data
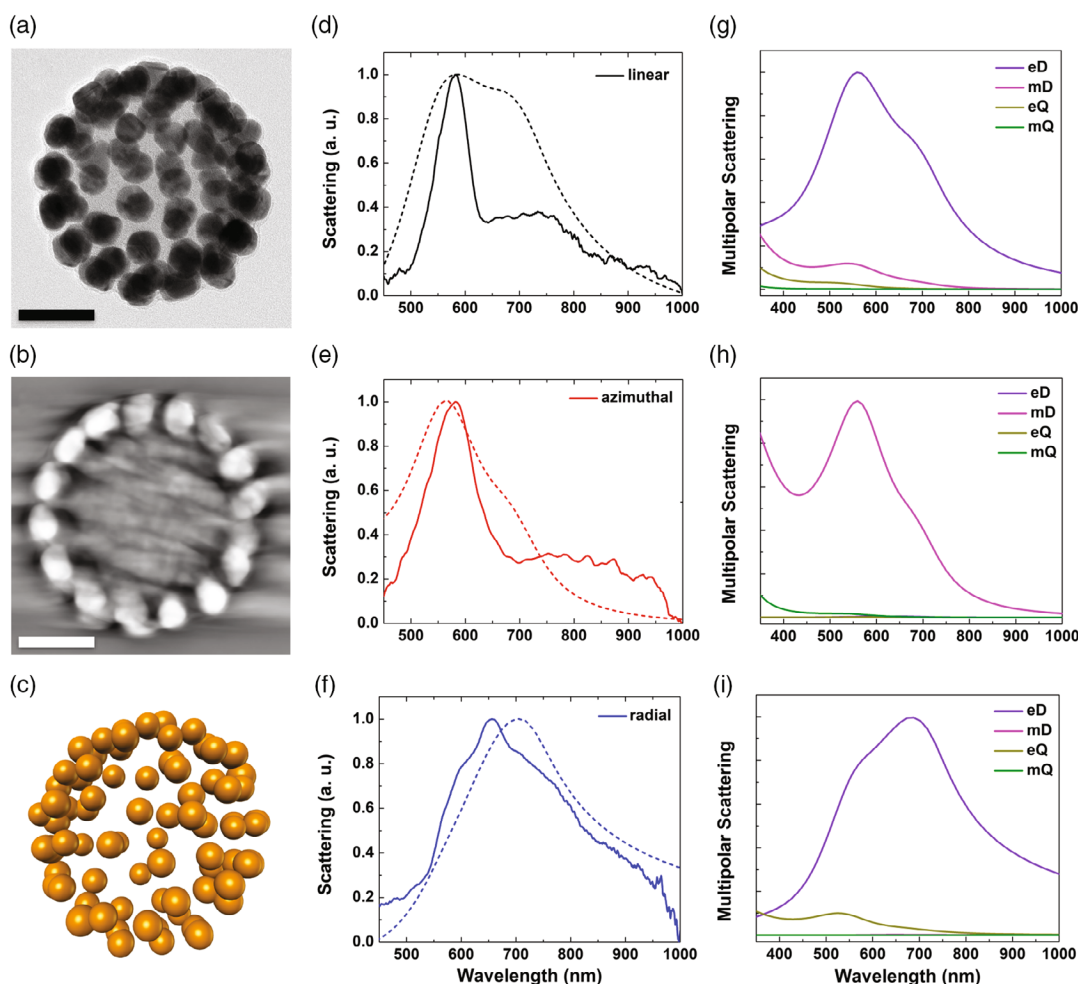
Figure 2. a–c) Characterization of a monolayer metamolecule. (a) 2D TEM image, (b) a tomogram slice of the equatorial plane, and (c) the 3D model of this particular monolayer metamolecule. A total of 76 particles are localized. Scale bars are 50 nm. d–f) Experimental (solid) and simulated (dashed) scattering spectra observed using (d) linearly, (e) azimuthally, and (f) radially polarized light excitation. g–i) Multipolar expansion of linear (g), azimuthal (h), and radial spectra (i) showing different selectivity for eD, mD, eQ, and mQ modes. The spectra obtained with linearly and radially polarized light (beams) are dominated by eD modes, while the azimuthal spectra are dominated by the mD modes of the metamolecule. (Note the different wavelength ranges used as the simulations could span a wider range than experimental measurements.)

(i.e., particle coordinates) shown in Figure 2 as input. We used both linearly polarized beams and vector beams to illuminate the metamolecules. Figure 2d–f shows the experimental (solid) and simulated (dashed) spectra of the metamolecule shown in Figure 2a. The experimental and simulated results are in excellent agreement. There are three main improvements compared to our former work.[20] The first is that the metamolecule is more homogeneous; that is, the AuNPs are well separated and not touching each other. Second, the AuNPs also adopt arrangements that tend toward an ordered (i.e., crystalline) layer as opposed to random. Third, the 3D structural information obtained by electron tomography enables precise comparison between the experiments and simulations.

To further understand the spectral features excited by different types of polarized light in these metamolecules, we performed a decomposition of the scattered far-fields into their electric and magnetic multipolar (e.g., dipolar and quadrupolar)

contributions, including electric dipole (eD), electric quadrupole (eQ), magnetic dipole (mD), and magnetic quadrupole (mQ) modes.[20,26] These intrinsic properties of the scattering are difficult to distinguish in the experimental spectra. Figure 2g–i shows the multipole analysis of the scattering spectra. The spectra resulting from excitation by linearly and radially polarized beams are dominated by the eD mode, while the spectra obtained with azimuthally polarized beams are dominated by optical magnetic modes. The higher order (e.g., quadrupole) modes are relatively weak as the overall size of the core–satellite metamolecule is small (150 nm dia.). These mode-specific excitations can be understood as governed by selection rules that depend on the polarization of the incident light and symmetry of the metamolecule. The radially polarized beam consists of pure electric propagating modes that uniquely couple to the metamolecule's electric scattering modes. By contrast, the azimuthally polarized beam consists of pure magnetic propagating modes that

uniquely couple to the metamolecule's magnetic scattering modes. The linearly polarized beam carries both electric and magnetic propagating modes, and therefore couples to all of the metamolecule's scattering modes.[26] Note that the sum of the modal-decomposed spectra is different from the total scattering spectra (e.g., Figure 2g vs d) due to the contribution of interferences between different modes (e.g., eD and eM or eD and eQ, etc.) in the total scattering spectra.

We also characterized metamolecules with multilayer structures by the same procedure as before. The structures and spectra of the multilayer metamolecule are shown in **Figure 3**. Note that the HAADF-STEM mode was used for electron tomography because the opacity of these metamolecules is greater than that of the metamolecule with a monolayer of AuNPs. Surprisingly, the spectra of multilayer metamolecules (both that shown in Figure 3 and others we measured; see the Supporting Information) are very similar to the spectra of monolayer metamolecules, and the electric/magnetic modes of each spectrum are nearly the

same. We measured many more metamolecules with different sizes, and metamolecules with bigger AuNPs (30 nm in diameter), and always found similar features of the spectra for each polarization excitation. These additional TEM images and scattering spectra are shown in Figure S2 and S3, Supporting Information. Therefore, we conclude that the outer shell dominates the plasmonic properties of the whole metamolecule and that the polarization properties of the beams selectivity drive electric or magnetic modes, or both, as described earlier. It should be noted that due to the overall size of the metamolecule being subwavelength, the eD mode dominates the spectral response corresponding to linear and radial beam illumination in the visible regime.[31] See the Supporting Information for additional results.

The experimental data/ TEM images of the gold nanoparticles in the "metamolecules" are not perfectly spherical. This is a general issue of the gold nanoparticles used in the chemical synthesis. However, the simulated spectra of Au nanoparticles (data not shown) agree very well with the measured spectra of a solution of
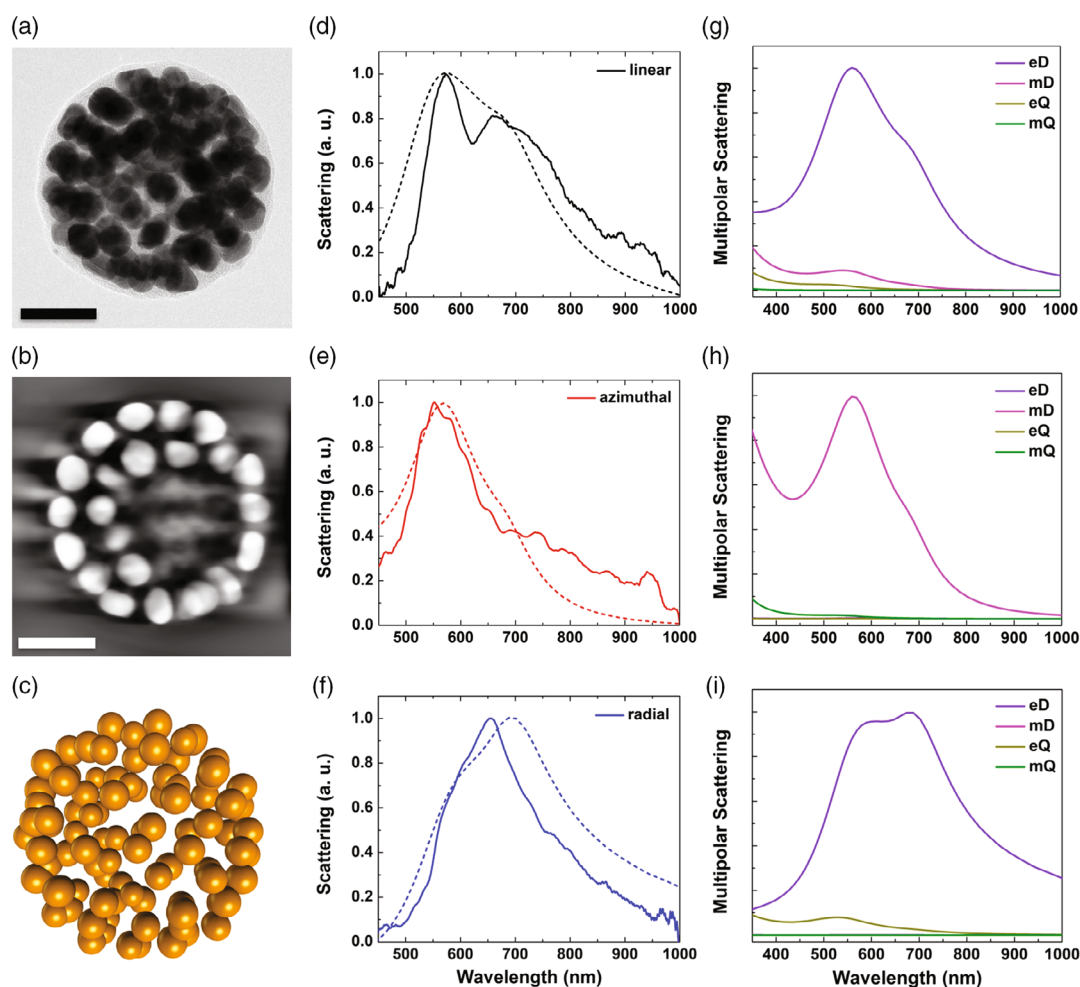

Figure 3. a–c) Characterization of a AuNP multilayer metamolecule. (a) 2D TEM image, (b) a tomogram slice of the equatorial plane, and (c) the 3D model of a multilayer metamolecule. A total of 93 particles were identified and their positions determined in 3D. Scale bars are 50 nm. d–f) Experimental (solid) and simulated (dashed) spectra by (d) linearly, (e) azimuthally, and (f) radially polarized light excitation. g–i) Multipolar expansion of (g) linear, (h) azimuthal, and (i) radial spectra showing different selectivity for eD, mD, eQ, and mQ modes. The spectra obtained using linearly and radially polarized light are dominated by eD modes, while the azimuthally polarized spectra are dominated by the mD mode of the metamolecule. The optical properties are very similar to those of the monolayer metamolecules.

the precursor single gold nanoparticles. Previous work in this field also treats these irregular shapes as spherical nanoparticles.[12,15] The irregularities may cause slight (red-)shifts of the peak position in absorption (extinction) spectra and possibly broadening of ensemble spectra. We judged that it would be virtually impossible to try to mimic the details of the individual particle shapes, as some of the irregularities in the tomographic images are a result of the imaging and reconstruction. Therefore, the excellent agreement of our simulated and measured extinction spectra of the metamolecules suggests that it is appropriate to use a model of spherical shape.

2.3. Scattering Spectra of Equatorial Regions of Metamolecules

To further understand the spectroscopic and plasmonic properties of the metamolecules, we performed FDTD simulations of selected (partial) regions of the metamolecules, specifically the ring of particles near the equator of the metamolecule versus the entire structure. **Figure 4** shows the results of simulations of the equatorial region of the metamolecules shown in Figure 2 and 3. The solid curves are the spectra of the equatorial region, and dashed curves are the spectra from the whole metamolecule. Note the two sets of scattering intensity scales for equatorial region and whole metamolecule simulations. The intensity of the equatorial spectra decreased due to there being fewer nanoparticles compared to the whole metamolecule. The intensity of the radial spectra decreased more than the others because the longitudinally polarized component of the focused radially polarized beam can excite the electric modes parallel to the propagation direction of the incident light in the whole metamolecule. However, these electric modes (centered around the "poles")

cannot be excited in the equatorial ring structure. Second, except for a slight blueshift of the equatorial spectra, the characteristics of the spectra from the equatorial region are similar to those of the whole metamolecule, particularly for the azimuthal case. Third, the modal decomposition analysis shows that the modes from these ring structures are eD for linearly and radially polarized beam excitations and mD for the azimuthally polarized excitation (see Figure S4, Supporting Information). These observations hold true for both the monolayer and multilayer metamolecules. Therefore, we conclude that the outer layer of the particles near the equator, that is, a monolayer ring structure, dominates the scattering spectra of the metamolecules. This is particularly true for azimuthally polarized beams and less so for radially polarized beams. These findings substantially agree with the earlier theoretical predictions by Engheta and coworkers on excitation of optical magnetism by azimuthally polarized beams of light.[32]

2.4. Reduced Backscattering from Mode Interference

We also analyzed the optical scattering signals from the backward and forward scattering directions by integrating the far-field radiation over the bottom and top hemispheres of the spherical monitor.[25] The results are shown in **Figure 5** and Figure S5, S6, Supporting Information. Figure 5a shows the results of multilayer and monolayer metamolecules. The backscattering is much weaker than the forward scattering for all polarization types. For example, the dominant scattering modes at short wavelength (e.g., 400 nm) are mD and mQ for azimuthal polarization beams interacting with multilayer metamolecules. The weak backscattering can be understood by looking at the spatial interference of these two modes, provided in the far-field intensity expression
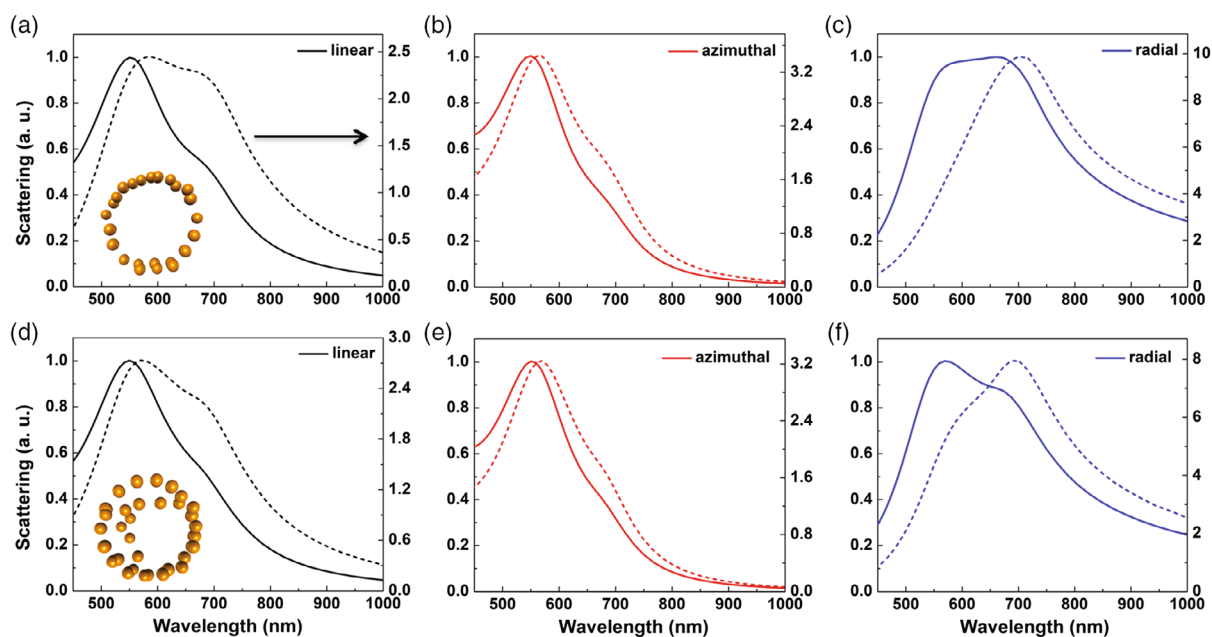

Figure 4. Simulated optical properties of the equatorial regions of the metamolecules. a–c) Scattering spectra for different polarized beams from the equatorial region of the monolayer metamolecule; d–f) equatorial region of multilayer metamolecule. The solid curves are the simulated spectra for the equatorial regions, and dashed curves are the simulated spectra for the whole metamolecule. The arrow in (a) indicates the scale for the dashed curve is on the right, and this is the same for all the dashed curves. The insets in (a) and (d) show the models of the equatorial regions of the monolayer metamolecule (a) and multilayer metamolecule (d).
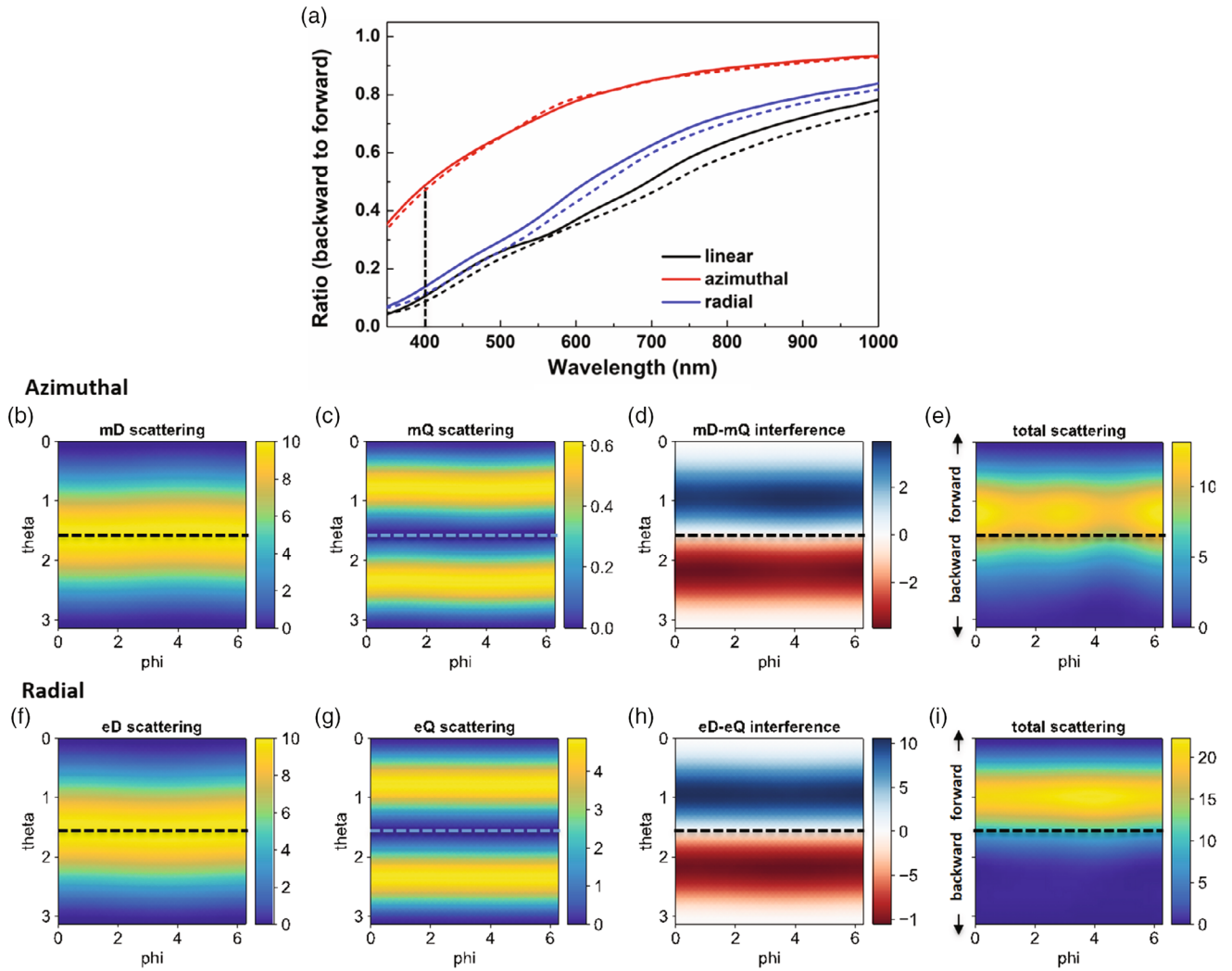
Figure 5. Angular scattering distributions obtained in simulations of the metamolecules. a) Ratio of backward to forward scattering by linear (black), azimuthal (red), and radial (blue) beam illumination. Solid curves are for the multilayer metamolecule and dashed curves are for the monolayer meta-molecule shown in Figure 2 and 3. b–e) Angular scattering (θ, Φ) intensity from azimuthally polarized beam excitation at 400 nm wavelength. These angular scales are in radians. Angular scattering of a z-oriented mD mode (b), the mQ mode (c), the interference term between mD and mQ modes (d), and total scattering (e). In (d), red denotes destructive interference and blue denotes constructive interference. The interference between the mD and mQ modes creates a spatial interference pattern that partially destructively interferes in the backward direction, which is the direction of the measurements. f–i) Angular scattering intensity from radially polarized beam excitation at 400 nm wavelength. Angular scattering of an eD mode (f), the eQ mode (g), the interference term between eD and eQ modes (h), and total scattering (i). The interference between the eD and eQ modes creates a spatial interference pattern that partially destructively interferes in the backward direction (direction of the measurements).

$$I_{\mathrm{azi}}(\theta,\phi) = |\vec{E}_{\mathrm{mD}} + \vec{E}_{\mathrm{mQ}}|^2 = |\vec{E}_{\mathrm{mD}}|^2 + |\vec{E}_{\mathrm{mQ}}|^2 + 2\mathrm{Re}\{\vec{E}_{\mathrm{mD}} \cdot \vec{E}_{\mathrm{mQ}}^*\}$$

$$(1)$$

In this equation, $\vec{E}_{\mathrm{mD}}$ and $\vec{E}_{\mathrm{mQ}}$ are the complex electric fields of the mD and mQ, respectively, at spherical coordinates θ and ϕ. The last term represents the spatial interference between these two modes, and can be positive (constructive) or negative (destructive). The analogous equation for the angle-dependent scattering from metamolecules interacting with radially polarized light is

$$I_{\mathrm{rad}}(\theta,\phi) = |\vec{E}_{\mathrm{eD}} + \vec{E}_{\mathrm{eQ}}|^2 = |\vec{E}_{\mathrm{eD}}|^2 + |\vec{E}_{\mathrm{eQ}}|^2 + 2\mathrm{Re}\{\vec{E}_{\mathrm{eD}} \cdot \vec{E}_{\mathrm{eQ}}^*\} \quad (2)$$

Figure 5b–e shows the angular distribution of the mD, mQ, the interference between mD and mQ, and the total scattering at 400 nm. The dashed horizontal lines in Figure 5b–e separate the forward and backward scattering. The red regions in Figure 5d correspond to destructive interference, while blue regions correspond to constructive interference. We also analyzed the interference for excitation with radially polarized light (Figure 5f–i) and linearly polarized beams (see Figure S5, Supporting Information), and at a longer wavelength of 700 nm (see Figure S6, Supporting Information). The results also exhibit almost complete destructive interference in backward scattering. In addition, the spectra obtained from azimuthally polarized

beam excitation show greater backscattering compared to excitation with linearly and radially polarized beams. This can be explained by the greater difference in the total scattering cross-sections of the mD and mQ modes shown in Figure 3h. Because the azimuthal beam selectively excites the mD and mQ modes, the only way to achieve reduced backscattering is through mD–mQ interference, which is therefore relatively small. In contrast, the linearly polarized beam has eD–mD interference and the radially polarized beam has eD–eQ interference, both of which are stronger than the corresponding mD–mQ interference in the azimuthally polarized beam case at 400 nm. Therefore, we conclude that the more comparable the scattering (cross-sections) of different modes that scatter from the metamolecules (at a given wavelength), the more reduced is the backscattering. Also, the backscattering from dipole and quadrupole modes exhibits an intensive π-phase shift, resulting in destructive interference of the associated field amplitudes.

We observe reduced backscattering ($\theta > \pi/2$) of the metamolecule at shorter visible wavelengths due to the spatial interference of multipolar modes for linearly polarized light and vector beams. Linearly polarized light has the least backscattering because the dipole modes are oriented along the polarization direction (x) and scatter and interfere in the backward ($-z$) direction. By contrast, the vector beams have z-oriented dipoles that scatter and interfere in transverse ($\theta \approx \pi/2$ or x,y) directions. The azimuthally polarized beam is seen to have more backscattered intensity than the other beams due to a much weaker mQ mode relative to the mD mode that results in less interference. Thus,

the vector beams allow control over the far-field angular radiation pattern by selective excitation of different multipolar modes.

2.5. Comparing the Core–Satellite to Similar-Sized Nanostructures

We compare the backscattering percentage of the core–satellite nanostructure to two other nanostructures of similar size: a 190 nm diameter gold sphere and a SiO_2 core (150 nm diameter)–Au shell (20 nm thickness). **Figure 6**a–c compares their backscattering for linear, radial, and azimuthal beam illumination, respectively. For the longer wavelengths 650–1000 nm, the core–satellite has the lowest back-scattering percentage for linear and radial beam illumination, while the core–satellite has the highest backscattering percentage for azimuthal beam illumination.

Core–satellite simulations were also performed by generalized Mie theory (GMT) that allowed interparticle coupling to be turned off so that the total scattering was a linear superposition of the individual dipole modes from the satellite Au particles (dashed curves). We found that the backscattering percentage is mostly insensitive to the coupling despite the significant scattering enhancement coupling causes (Figure S9, Supporting Information), suggesting that the backscattering percentage is largely determined by the geometric placement of the Au nanoparticles.

For radial (azimuthal) beam illumination, there are two excited modes: electric (magnetic) dipole and electric (magnetic)
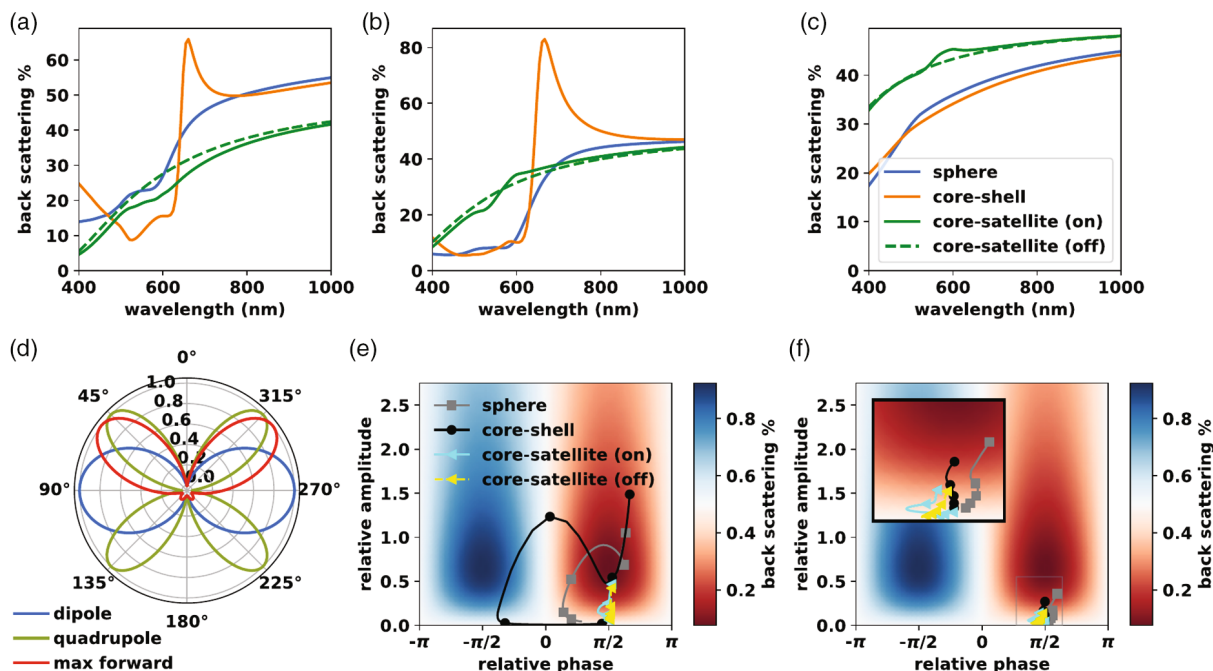

Figure 6. The relative amplitude and phase of dipole and quadrupole modes control the backscattering percentage for different nanostructures. a–c) Backscattering percentage of a Au sphere (190 nm diameter, blue), SiO_2 core (150 nm diameter)–Au shell (20 nm thickness, orange), and core–satellite monolayer nanostructure with and without coupling interactions (green) for linearly (a), radially (b), and azimuthally (c) polarized beam illumination. d) Far-field angular scattering patterns of the dipole (blue), quadrupole (green), and a linear combination of dipole and quadrupole achieving a maximum forward scattering of ≈92% (red). e,f) The relative amplitude and phase of the dipole and quadrupole modes for the different nanostructures determine the amount of backscattering for radially (e) and azimuthally (f) polarized beam illumination. Each curve corresponds to the 400–1000 nm wavelength range for the given nanostructure.

quadrupole modes. Consequently, only the relative amplitude and phase of these two modes determine the percentage of backscattered light. Figure 6d shows the far-field angular scattering of these dipole and quadrupole modes, as well as the combination of these two modes that achieves the maximum possible forward scattering (92%). This condition is met when the relative phase is $\phi_Q - \phi_D = \pi/2$ and the relative amplitude is $A_Q/A_D \approx 0.67$. Figure 6e,f shows the dependence of the backscattering percentage on the relative amplitude and phase. Each curve corresponds to one of the nanostructures in the 400–1000 nm wavelength range for radial (e) and azimuthal (f) beam illuminations. While the sphere and core–shell structures exhibit rapid changes in the relative phase for radially polarized beam illumination, the core–satellite maintains a phase difference close to the optimal $\pi/2$ that enables it to achieve lower broadband backscattering.

3. Conclusion

We have demonstrated an approach that combines several techniques, including single particle spectroscopy with vector beams, electron tomography, particle localization, and electrodynamics simulations, to study the optical properties of complex plasmonic metamolecules. We found that these nanoordered metamolecules exhibit reduced backscattering. The collective plasmonic scattering spectral properties of the metamolecules dominantly arise from the ring structure in the equatorial region of the structure. These metamolecules will be good candidate building blocks of metasurfaces that exhibit reduced reflectivity, especially at shorter optical wavelengths. Ordered arrays can be fabricated by surface-directed assembly on patterned templates.[33] Although we studied single core–satellite metamolecules, the approach we present can be extended to other nanostructures. Therefore, the approach and insights into the collective electromagnetic excitations and scattering we present opens the way to systematically study the plasmonic properties of complex nanostructures and their properties as metamaterials and could have various photonic applications, including solar collection.

4. Experimental Section

Materials: Amino-terminated 1,2-polybutadiene (PB-NH$_2$, $M_n = 3.0$ kg mol^{-1}, $M_w/M_n = 1.11$) was purchased from Polymer Source, Inc. (Canada). PS ($M_n = 280$ kg mol^{-1}, $M_w/M_n = 2.12$) was purchased from Aldrich (St. Louis, USA). Tetrahydrofuran (THF, with stabilizer) and polyethylene glycol (PEG, average molecular weight = 6 kg mol^{-1}) were purchased from Wako Pure Chemical Industries (Tokyo, Japan). Aqueous dispersions of negatively charged AuNPs with average diameters of 20 and 30 nm were purchased from British Bio Cell International (Cardiff, UK). All polymers, reagents, and AuNPs were used as received without further purification.

Preparation of PS/PB-NH$_2$ Core–Shell Polymer Particles: Polymer particles with core–shell phase-separated structures were prepared by SORP.[27] The thickness of the shell depended entirely on the PB-NH$_2$ content, which is consistent with the increase of the PB-NH$_2$ content. THF solutions of PS and PB-NH$_2$ were prepared at a concentration of 0.1 mg mL^{-1}, and each polymer solution was mixed in a glass bottle at 90:10 ratios of PB-NH$_2$:PS for multilayer metamolecules and 70:30 for monolayer metamolecules, respectively. Membrane-filtered water (1 mL, Milli-Q, Millipore, Billerica, USA) was added to the polymer mixture at 1 mL min^{-1} with constant stirring at 500 rpm and the resulting mixture was then allowed to stand at 40 °C in a water bath to evaporate the THF. The solubility of the polymers

in the THF/water solvent decreased as the THF evaporated and the polymers precipitated as particles. Complete evaporation of THF produced an aqueous dispersion of polymer particles.

Incorporation of AuNPs into the Core–Shell Polymer Particles: A prepared polymer particle aqueous dispersion (100 µL, 0.01 mg mL^{-1}), the aqueous dispersion of AuNPs (200 µL), and an aqueous PEG solution (100 µL, 1.0 mg mL^{-1}) were placed in a plastic microtube. The mixture was kept at room temperature for 1 h without stirring. For electron microscope measurements, the PB-NH$_2$ moieties of the polymer particles were stained with OsO$_4$ (Wako Pure Chemical Industries). An aqueous OsO$_4$ solution (0.2 wt%) was added to the aqueous dispersion of composite particles. After 2 h, the free AuNPs and excess OsO$_4$ were removed by three cycles of centrifugation (12 000 rpm, 5 min, 5 °C) and washing with membrane-filtered water. The separated composite particles were redispersed in membrane-filtered water.

Measurements of Scattering Spectra of PS-AuNP Metamolecules: The scattering spectra were measured using a home-built microscopy setup. A schematic of the vector beam spectroscopy setup was published elsewhere.[20,25] Briefly, a spatially coherent (broadband) white light continuum (Fianium, White Lase SC400, from 450 to 1000 nm) was coupled to an inverted optical microscope equipped with an oil immersion objective with numerical aperture NA ≤ 1.4 (Olympus, IX-81; SAPO 100X). The vector beam generator was placed outside the microscope, just after the linear polarizer, and positioned using a fine adjustment translation stage. The vector beam generator used was a liquid-crystal based polarization converter (ARCoptix, Switzerland), which can generate azimuthally and radially polarized cylindrical vector beams.[28] The images and spectra of the light backscattered from the metamolecule (sample plane) were recorded either by a sCMOS array detector (Andor, Neo) connected to the eyepiece of the microscope or by an EM CCD (Andor, Newton) connected to an imaging spectrometer (Andor Shamrock 193i) coupled to the side port of the microscope. The halogen light source (on the top) was coupled to an optical fiber and microscope objective to illuminate the samples. The aqueous dispersion of nanoparticles was dropcast on formvar-coated TEM finder grids and dried overnight.

Correlated single particle spectroscopy and TEM structure measurements were conducted of specific metamolecules. Before taking scattering spectra, moderate resolution TEM survey images were acquired using a Tecnai F30 (FEI) with the accelerating voltage of 300 kV. The grid was then placed on a glass cover slide. Subsequently, glycerol ($n = 1.47$) was put on top of the grid to match the index of the glass slide. Glycerol was used because it can be easily removed for electron tomography after optical measurements. The sample chamber was closed with another cover slide on top, forming a sandwich structure with the grid between two glass slides. Note that the metamolecules chosen for measurements were well separated from other metamolecules (≈5 µm), to avoid scattering from neighbor particles that could affect the measurements, and also to more easily acquire tilt series images in electron tomography.

Electron Tomography and Particle Localization: After finishing the optical measurements, the grid was dried overnight in vacuum. Electron tomography was conducted on a TEM (Tecnai F30) equipped with a high-tilt rotating sample holder. A tilt series of TEM images of the monolayer metamolecule (in Figure 2) was acquired at angles ranging from 70° to −70° at an angular interval of 1° at an accelerating voltage of 300 kV. The tilt images were aligned and reconstructed using the IMOD software package using the SIRT.[30] After reconstruction, the data stack was filtered using a low-frequency Fourier filter (IMOD) and contrast inverted to give light particles with a dark background to enable individual particle identification. For the multilayer metamolecule, the HAADF-STEM mode was used to acquire tilt series images with a better signal-to-noise ratio than is possible by standard TEM mode. Videos of the tile series and orthogonal slices for both the monolayer and multilayer metamolecules are shown in Video S1–S4, Supporting Information.

To determine the coordinates of the center and diameter of each gold nanoparticle, 3D particle localization was performed using the Crocker and Grier algorithm.[29] The full 3D experimental structural information of the core–satellite metamolecules was used to create a 3D model structure for the electrodynamics simulations.

Simulations of PS–AuNP Metamolecules: Simulations of the PS–AuNP metamolecules were performed using the FDTD method[34] via a freely available software package MEEP.[35] Figure 1 shows a diagram of the simulation box. PS–AuNP metamolecules were placed in an index 1.47 environment with positions (and gaps) obtained from TEM electron tomography. The dielectric function of gold was obtained by fitting a Drude–Lorentz model to the Johnson–Christy dielectric measurements of gold.[36] For each simulation, the incident source had a given polarization state (linear, radial, or azimuthal) and a Gaussian temporal envelope chosen to span the incident wavelengths from 350 to 1000 nm. A spatial envelope was chosen to give each beam a diameter of 300 nm (for the linearly polarized beam, this is the width of the Gaussian; for the CVBs, this is the size of the maximum intensity of the doughnut cross-sectional amplitude). A perfectly matched layer (PML) was used at the boundary of the simulation domain to mimic an open boundaryless system. The simulation was then time-stepped until the fields decayed and the scattering spectra converged.

The scattered electric field components were collected on the surface of a spherical monitor that encompassed the PS–AuNP metamolecule. These electric field components were used to compute a multipole expansion of the scattered radiation by projecting the electric field onto a set of orthogonal vector spherical harmonic wave (VSHW) functions[26,37,38]

$$a_{nm} = \frac{\int_0^{2\pi}\int_0^\pi \boldsymbol{E}_{\text{scat}} \cdot \boldsymbol{N}_{nm}^* \sin\theta \mathrm{d}\theta \mathrm{d}\phi}{\int_0^{2\pi}\int_0^\pi |\boldsymbol{N}_{nm}|^2 \sin\theta \mathrm{d}\theta \mathrm{d}\phi} \tag{3}$$

$$b_{nm} = \frac{\int_0^{2\pi}\int_0^\pi \boldsymbol{E}_{\text{scat}} \cdot \boldsymbol{M}_{nm}^* \sin\theta \mathrm{d}\theta \mathrm{d}\phi}{\int_0^{2\pi}\int_0^\pi |\boldsymbol{M}_{nm}|^2 \sin\theta \mathrm{d}\theta \mathrm{d}\phi} \tag{4}$$

Here, a_{nm} and b_{nm} are the electric and magnetic multipole scattering coefficients, respectively, of order n and spherical orientation m. Physically, $n = 1$ corresponds to the dipole modes, $n = 2$ corresponds to the quadrupole modes, etc. and $m = -n, -n+1, \ldots, 0, \ldots n-1, n$ specifies different orientations of the mode. The complex vector fields $\boldsymbol{N}_{nm}$ and $\boldsymbol{M}_{nm}$ are the electric and magnetic VSHW functions, respectively.

The total scattering cross-section was then computed as a sum over the individual multipolar scattering coefficients

$$C_{\text{sca}} = k^2 \sum_{n=1}^\infty \sum_{m=-n}^n n(n+1)(|a_{nm}|^2 + |b_{nm}|^2) \tag{5}$$

Here, k is the wavenumber of the incident radiation in the oil medium. Each term in the sum represents the multipolar scattering cross-section of a particular multipolar mode.

This angular analysis method was used for scattered radiation up to quadrupole order for both electric and magnetic modes. Figure 2 and 3 show the multipole expansion results for the PS–AuNP metamolecule. Equation (3) and (4) also allow the fields to be projected into the far field, from which angular scattering quantities can be computed. To determine spectra in the back scattering direction to mimic the experiments, the far-field Poynting vector was integrated over the cap of a cone with apex angle 140°, oriented in the backward ($\theta = \pi$) direction to match the range of angles associated with the experimental N.A. Figure 2 and 3 show simulated backscattering spectra in comparison with experiment. The backward to forward scattering ratios in Figure 5 were obtained by integrating the far field over the full bottom and top hemispheres (apex angle 180°).

Generalized Mie Theory (GMT) Simulations: The GMT[39] was used to simulate the core-satellite meta-molecule with interactions turned on and off (Figure 6). In GMT, each particle is represented by a collection of scattering multipolar modes, $\boldsymbol{p}_i^{\text{scat}}$. For N particles, these scattering modes are coupled to one another through an interaction matrix A_{ij} by the equation $\boldsymbol{p}_i^{\text{scat}} = A_{ij}\boldsymbol{p}_j^{\text{inc}}$, where $\boldsymbol{p}_j^{\text{inc}}$ are the incident multipolar modes of the beam at each particle.[40] To disable particle interactions, we set the interaction matrix to the identity matrix, $A_{ij} = \delta_{ij}$. With interactions disabled, the angular far-field is a coherent sum of non-interacting dipoles that includes interference effects due to the spatial separation of the particles. With interactions enabled, the induced dipole of each particle is modified by the scattered fields of all the other particles, which includes near-field coupling and many-body interactions.

Supporting Information

Supporting Information is available from the Wiley Online Library or from the author.

Conflict of Interest

The authors declare no conflict of interest.

Author Contributions

T.-S.D. and J.P. contributed equally to this work. T.-S.D., H.Y., and N.F.S. designed the experimental aspects of the research. Y.H. prepared the core–satellite metamolecules. T.-S.D. performed the optical measurements, electron tomography, and particle tracking. J.P. performed the simulations. N.S. helped in performing optical measurements. T.-S.D., J.P., and Y.H. analyzed the data. T.-S.D., J.P., H.Y., and N.F.S. wrote the manuscript. H.Y. and N.F.S. supervised the project. All authors discussed the results and commented on the manuscript.

[1] J. B. Pendry, A. Aubry, D. R. Smith, S. A. Maier, *Science* **2012**, *337*, 549.

[2] Z. J. Wong, Y. Wang, K. O'Brien, J. Rho, X. B. Yin, S. Zhang, N. Fang, T. J. Yen, X. Zhang, *J. Opt.* **2017**, *19*, 084007.

[3] O. Hess, J. B. Pendry, S. A. Maier, R. F. Oulton, J. M. Hamm, K. L. Tsakmakidis, *Nat. Mater.* **2012**, *11*, 573.

[4] N. Meinzer, W. L. Barnes, I. R. Hooper, *Nat. Photonics* **2014**, *8*, 889.

[5] N. F. Yu, F. Capasso, *Nat. Mater.* **2014**, *13*, 139.

[6] S. Gwo, H. Y. Chen, M. H. Lin, L. Y. Sun, X. Q. Li, *Chem. Soc. Rev.* **2016**, *45*, 5672.

[7] G. Li, S. Zhang, T. Zentgraf, *Nat. Rev. Mater.* **2017**, *2*, 17010.

[8] M. L. De Marco, S. Semlali, B. A. Korgel, P. Barois, G. L. Drisko, C. Aymonier, *Angew. Chem., Int. Ed.* **2018**, *57*, 4478.

[9] Z. L. Wu, Y. B. Zheng, *Adv. Opt. Mater.* **2018**, *6*, 1701057.

[10] J. Valentine, S. Zhang, T. Zentgraf, E. Ulin-Avila, D. A. Genov, G. Bartal, X. Zhang, *Nature* **2008**, *455*, 376.

[11] F. Shafiei, F. Monticone, K. Q. Le, X. X. Liu, T. Hartseld, A. Alu, X. Q. Li, *Nat. Nanotechnol.* **2013**, *8*, 95.

[12] S. N. Sheikholeslami, H. Alaeian, A. L. Koh, J. A. Dionne, *Nano Lett.* **2013**, *13*, 4137.

[13] A. Kuzyk, R. Schreiber, H. Zhang, A. O. Govorov, T. Liedl, N. Liu, *Nat. Mater.* **2014**, *13*, 862.

[14] S. Yang, X. J. Ni, X. B. Yin, B. Kante, P. Zhang, J. Zhu, Y. Wang, X. Zhang, *Nat. Nanotechnol.* **2014**, *9*, 1002.

[15] Z. X. Qian, S. P. Hastings, C. Li, B. Edward, C. K. McGinn, N. Engheta, Z. Fakhraai, S. J. Park, *ACS Nano* **2015**, *9*, 1263.

[16] J. Sharma, R. Chhabra, A. Cheng, J. Brownell, Y. Liu, H. Yan, *Science* **2009**, *323*, 112.

[17] L. Malassis, P. Masse, M. Treguer-Delapierre, S. Mornet, P. Weisbecker, V. Kravets, A. Grigorenko, P. Barois, *Langmuir* **2013**, *29*, 1551.

[18] J. Lee, J. H. Huh, K. Kim, S. Lee, *Adv. Funct. Mater.* **2018**, *28*, 1707309.

[19] M. Kanahara, H. Satoh, T. Higuchi, A. Takahara, H. Jinnai, K. Harano, S. Okada, E. Nakamura, Y. Matsuo, H. Yabu, *Part. Part. Syst. Charact.* **2015**, *32*, 441.

[20] U. Manna, J. H. Lee, T. S. Deng, J. Parker, N. Shepherd, Y. Weizmann, N. F. Scherer, *Nano Lett.* **2017**, *17*, 7196.

[21] D. L. Liu, F. Zhou, C. C. Li, T. Zhang, H. H. Zhang, W. P. Cai, Y. Li, *Angew. Chem., Int. Ed.* **2015**, *54*, 9596.

[22] A. Sanchez-Iglesias, M. Grzelczak, T. Altantzis, B. Goris, J. Perez-Juste, S. Bals, G. Van Tendeloo, S. H. Donaldson, B. F. Chmelka, J. N. Israelachvili, L. M. Liz-Marzan, *ACS Nano* **2012**, *6*, 11059.

[23] K. D. Osberg, N. Harris, T. Ozel, J. C. Ku, G. C. Schatz, C. A. Mirkin, *Nano Lett.* **2014**, *14*, 6949.

[24] L. Weller, V. Thacker, V. L. O. Herrmann, E. A. Hemmig, A. Lombardi, U. F. Keyser, J. J. Baumberg, *ACS Photonics* **2016**, *3*, 1589.

[25] T. S. Deng, J. Parker, Y. Yifat, N. Shepherd, N. F. Scherer, *J. Phys. Chem. C* **2018**, *122*, 27662.

[26] J. Parker, S. Gray, N. F. Scherer, arxiv: 1711.06833, **2017**.

[27] M. Kanahara, M. Shimomura, H. Yabu, *Soft Matter* **2014**, *10*, 275.

[28] M. Stalder, M. Schadt, *Opt. Lett.* **1996**, *21*, 1948.

[29] J. C. Crocker, D. G. Grier, *J. Colloid Interface Sci.* **1996**, *179*, 298.

[30] J. R. Kremer, D. N. Mastronarde, J. R. McIntosh, *J. Struct. Biol.* **1996**, *116*, 71.

[31] A. A. R. Neves, D. Pisignano, *Opt. Lett.* **2012**, *37*, 2418.

[32] A. Alù, A. Salandrino, N. Engheta, *Opt. Express* **2006**, *14*, 1557.

[33] X. Y. Liu, S. Biswas, J. W. Jarrett, E. Poutrina, A. Urbas, K. L. Knappenberger, R. A. Vaia, P. F. Nealey, *Adv. Mater.* **2015**, *27*, 7314.

[34] A. Taflove, S. C. Hagness, *Computational Electrodynamics: The Finite-Difference Time-Domain Method*, 3rd ed., Artech House, Boston **2004**.

[35] A. F. Oskooi, D. Roundy, M. Ibanescu, P. Bermel, J. D. Joannopoulos, S. G. Johnson, *Comput. Phys. Commun.* **2010**, *181*, 687.

[36] P. B. Johnson, R. W. Christy, *Phys. Rev. B* **1972**, *6*, 4370.

[37] P. Grahn, A. Shevchenko, M. Kaivola, *New J. Phys.* **2012**, *14*, 093033.

[38] S. Mühlig, C. Menzel, C. Rockstuhl, F. Lederer, *Metamaterials* **2011**, *5*, 64.

[39] Y.-L. Xu, *Appl. Opt.* **1995**, *34*, 4573.

[40] T. A. Nieminen, H. Rubinsztein-Dunlop, N. R. Heckenberg, *J. Quant. Spectrosc. Radiat. Transfer* **2003**, *79*, 1005.